PHYSICAL REVIEW A VOLUME 20, NUMBER 3 SEPTEMBER 1979

Generalized quantum defects: Their variations with energy and radius

Chris H. Greene

Department of Physics, University of Chicago, Chicago, Illinois 60637

(Received 26 March 1979)

A unified interpretation of single-channel quantum-defect behavior is presented, and illustrated with the example of a square well. As an application the quantum defects for the lowest three partial waves of potassium are calculated and discussed as continuous functions of the energy above, near, and far below the ionization threshold, with emphasis on their non-Rydberg spectral properties; results for other atoms are discussed. The quantum defect for the radial motion of a $^1P^\circ$ electron pair of H^- is also calculated, thereby combining Macek's hyperspherical-coordinate approach with quantum-defect theory.

I. INTRODUCTION

The study of phase shifts has played an increasingly important role in the unraveling of complicated dynamics in diverse atomic processes. The energy dependence of scattering and photoabsorption cross sections and especially their resonant behavior have usually been interpreted in terms of the variations of a small number of contributing phase shifts. While the approximate evaluation of phase shifts for any given potential has become a routine numerical task, a unified view of their dependence on the potential field and on the energy throughout the spectrum is only beginning to emerge. A recent paper by Fano, Theodosiou, and Dehmer[1] (referred to below as FTD) has surveyed the zero energy ($\epsilon = 0$) phase shifts of atomic electrons, showing a number of prominent, systematic variations in the dependence of δ_l on angular momentum l and on the strength and range of the potential.

The present study has grown out of an attempt to better understand the mechanisms contributing to these and other properties. Additional systematics appear in the energy dependence of phase shifts both above and far below thresholds, and in their dependence on the type of long-range interaction between particles. (FTD allowed only for a long-range Coulomb field and $\epsilon = 0$.) This last item posed the new problem of comparing different long-range fields on an equal footing. Its solution required a substantial effort in its own right and was reported quite recently in a paper referred to below as I.[2]

The main goal of this work is the construction of a unified framework for interpreting properties of single-channel phase shifts (or the equivalent quantum defects $\mu_l \equiv \delta_l/\pi$) as functions of energy. This has required a lengthy introduction and development of several new concepts. As illustrative examples the quantum defects are calculated for several different atomic fields and orbital momenta in the Hartree-Slater approximation as continous functions of the energy from -50 to $+5$ keV. This study, whose initial findings have already appeared in a preliminary report,[3] complements the FTD[1] and other studies[4] of phase-shift variations with atomic number. It further identifies four characteristic energy regions (I–IV) in which the quantum defect has different qualitative features (see Fig. 1). For example, region II of the spectrum contains the Rydberg series. Our unified treatment thus serves to describe quite different dynamical systems. This is illustrated by another, quite unrelated example, which obtains the quantum defect for the radial motion of a pair of electrons in H^-. The calculation of H^- phase shifts complements the studies of two-electron correlations by Macek, Lin, and Fano[5] over the past decade, and represents the first explicit combination of their hyperspherical-coordinate method with quantum-defect-theory (QDT) methods.

Further motivation of the present work stems from an inadequate understanding of the mechanism responsible for the termination of Rydberg series at their lower end.[6] That is, while the Rydberg formula (in a.u.) $\epsilon_n = -\frac{1}{2}(n - \mu_l)^{-2}$ is valid for arbitrarily large integers n, it is not immediately clear from the formalism why it "cuts off" at some integer n (e.g., $n \geq 4$ for $l = 0$ atomic potassium). An initial study of this topic was made by Seaton[7] long ago. Sections III and IV demonstrate that the quantum defect can be constructed as a continuous function of energy even far below an ionization threshold, and secondly that the series termination is often accompanied by a dramatic stair-step dependence of μ_l on energy [see Fig. 7(a)]. These rapid changes of the quantum defect relate in turn to its r dependence as described by the phase-amplitude method (PAM),[1,8] in which μ_l is regarded as the limit of a continuous radial function $\mu_l(r)$ for $r \to \infty$. The earlier studies[1,8] showed that $\mu_l(r)$ often increases in a

© 1979 The American Physical Society

stepwise fashion as r increases, though they did not account in detail for the rapid radial steps. A major goal of Secs. III and IV is to describe the mechanism causing the radial steps in $\mu_l(r)$, to show that this same mechanism causes a stair-step energy dependence of $\mu_l(\infty)$ far below threshold, and more generally to show that the phase-shift dependence on r gives valuable insight into the short-range dynamics. This connection is then developed one step further by plotting μ_l as a surface depending on both parameters ϵ and r, showing at a glance the characteristic Rydberg and non-Rydberg spectral properties of μ_l.

The paper is organized as follows. Section II summarizes the relevant features of the extended QDT presented in I and of the phase-amplitude formulation. Section III describes characteristic classes of quantum-defect behavior with special reference to the illustrative example of an $l=0$ square well. These ideas are then applied to the discussion of two quite different dynamical systems in Sec. IV. The atomic quantum defects are calculated in Sec. IV A, primarily for neutral potassium, but an indication of the dependence of $\mu_{l=0}$ on atomic number and shell structure is provided by results for sodium, aluminum, and phosphorus. At the end of Sec. IV A the termination of the lower end of the Rydberg series is discussed in the context of the earlier results. Finally Sec. IV B combines QDT with the hyperspherical-coordinate approach[5] for analyzing the levels of two strongly correlated electrons. Specifically, the quantum defects are evaluated for the the ${}^1P^0$ "sp−" series of Feshbach resonances in H$^-$ which converge to the $n=2$ level of hydrogen. Various properties of the resulting "dipole-field series" are then compared and contrasted with Rydberg-series properties.

II. FORMULATION SUMMARY

The starting point for both single- and multichannel QDT applications is the Schrödinger equation for a particle moving in a spherically symmetric potential (in a.u.),

$$\left(-\frac{1}{2}\frac{d^2}{dr^2}+V(r)+\frac{l(l+1)}{2r^2}-\epsilon\right)P(\epsilon,l,r)=0\,. \quad (2.1)$$

For the interesting physical systems the large-r form of the potential is a simple analytic function which we denote by $V_0(r)$. As discussed in I, $V_0(r)$ can be taken to be one of the three basic fields:

Potential	$V_0(r)$
Zero field	0
Coulomb	$-1/r$
"Dipole"	$-\frac{1}{2}(a^2+\frac{1}{4})/r^2$

(2.2)

Any shorter-range potential than r^{-2} can be regarded (in first approximation) as an example of zero field, because it does not have an infinite series of bound levels. [Section II E of I discusses this point further. See especially the discussion of Eqs. (2.81) and (2.82) in I.] In the treatment below we have assumed that beyond some core radius r_0 the potential $V(r)$ reduces exactly to one of the large-r forms $V_0(r)$ in Eq. (2.2).

Three independent base pairs satisfying Eq. (2.1) were discussed in I for each of the three potentials in Eq. (2.2); the most important of their properties are summarized in its Table I. Here we summarize those base pair properties most important to the problem at hand:

(i) The base pair (f^0,g^0) is normalized to be independent of energy near $r=0$. Excluding the dipole potential, this means that as $r\to 0$

$$f^0\sim r^{l+1},\quad g^0\sim r^{-l},\quad\text{and}\quad W(f^0,g^0)=2/\pi\,. \quad (2.3)$$

Most important for our purposes, these functions—as well as the phase shifts referred to them—are analytic in the energy ϵ at all finite r. The analytic base pair for the dipole field is also energy independent near $r\sim 0$, but the simple power laws of Eq. (2.3) are not realistic since the roots of the indicial equations are complex.

(ii) The solutions (f^+,f^-) are chosen to be outgoing and incoming wave for $\epsilon>0$,

$$f^\pm \xrightarrow[r\to\infty]{} e^{\pm ikr}r^{\pm\zeta}\,, \quad (2.4a)$$

where $\zeta=i/k$ for the Coulomb field and vanishes otherwise, and $k^2=2\epsilon$. At negative energies $k\to i/\nu$ and the effective quantum number ν becomes the energy variable. Correspondingly when $\epsilon=-\frac{1}{2}\nu^{-2}<0$,

$$f^\pm \xrightarrow[r\to\infty]{} e^{\mp r/\nu}r^{\pm\zeta}\,. \quad (2.4b)$$

The Wronskian of this pair is $W(f^+,f^-)=2/\nu$.

(iii) The base pair (f,g) is energy normalized for $\epsilon>0$, and its members oscillate 90° out of phase at large r:

$$f(\epsilon,l,r)\xrightarrow[r\to\infty]{}(2/\pi k)^{1/2}\sin[kr-i\zeta\ln r+\eta(k,l)]\,,$$

$$g(\epsilon,l,r)\xrightarrow[r\to\infty]{}-(2/\pi k)^{1/2}\cos[kr-i\zeta\ln r+\eta(k,l)]\,,$$

where

$$\eta(k,l)=\begin{cases}-l\pi/2 & \text{(zero field)}\\ -l\pi/2+k^{-1}\ln 2k+\arg\Gamma(l+1-i/k) & \text{(Coulomb)},\\ -\pi/4+\phi(k,a) & \text{(dipole)}\end{cases} \quad (2.5a)$$

and where $\phi(k,a)$ is defined in Table I of I. [In these expressions $\eta(k,l)$ is meant to be interpreted as $\eta(k,a)$ for the dipole field.] At negative energies, $\epsilon<0$, the energy-normalized base pair (f,g) is related to the pair $(\nu/\pi)^{1/2}(Df^+, D^{-1}f^-)$ by an orthogonal transformation:

$$f(\epsilon,l,r)=(\nu/\pi)^{1/2}[\sin\beta_l(\nu)D^{-1}f^- - \cos\beta_l(\nu)Df^+]\,,$$
$$g(\epsilon,l,r)=-(\nu/\pi)^{1/2}[\cos\beta_l(\nu)D^{-1}f^- + \sin\beta_l(\nu)Df^+]\,, \tag{2.5b}$$

where

$$\beta_l(\nu)=\begin{cases}\pi/4 & \text{(zero field)}\\ \pi(\nu-l) & \text{(Coulomb field)}\\ a\ln 2\nu-\arg\Gamma(1-ia) & \text{(dipole field)}\end{cases}\,, \tag{2.6}$$

and where $D(\nu,l)$ is defined for each field in Table I of I.

It will be convenient in Secs. III and IV to have an explicit form for the transformation from (f,g) to (f^0,g^0). The result is

$$\begin{pmatrix} f\\ g\end{pmatrix}=\begin{pmatrix}A^{1/2} & 0\\ A^{-1/2}\mathcal{G} & A^{-1/2}\end{pmatrix}\begin{pmatrix}f^0\\ g^0\end{pmatrix},\quad \epsilon<0 \tag{2.7}$$

where $A(\nu,l)$ is replaced at $\epsilon>0$ by a different parameter $B(\epsilon,l)$. The explicit expressions for these coefficients are given in Table I of I.

Because $V(r)=V_0(r)$ for all $r\geq r_0$, the solution $P(\epsilon,l,r)$ of Eq. (2.1) can be written in this range as a superposition of any chosen base pair of independent solutions of the outer field; for example, if (f,g) are used,

$$P(\epsilon,l,r)=\gamma_{\epsilon l}[f(\epsilon,l,r)\cos\pi\mu_{\epsilon l} - g(\epsilon,l,r)\sin\pi\mu_{\epsilon l}],\quad r\geq r_0\,. \tag{2.8}$$

The quantum-defect theory makes use of the fact that $\mu_{\epsilon l}$ completely characterizes the effect of the inner field on the outer-field wave function. To illustrate, the normalization is determined by

$$\gamma_{\epsilon l}^2=1,\quad \epsilon>0$$
$$\gamma_{\epsilon_n l}^{-2}=\pi^{-1}\frac{d}{d\epsilon}[\beta_l(\nu)+\pi\mu_{\epsilon l}]\Big|_{\epsilon=\epsilon_n},\quad \epsilon<0\,, \tag{2.9}$$

where the bound-state eigenvalues are the solutions of

$$\beta_l(\nu_n)+\pi\mu_{\epsilon_n l}=n\pi\,. \tag{2.10}$$

This reduction of the single-channel problem to the calculation of a single parameter $\mu_{\epsilon l}$ is the essence of the quantum-defect method.

The quantum defect can be expressed formally in terms of the three functions (f,g) and P using Wronskians [recall $W(a,b)\equiv ab'-a'b$]:

$$\tan\pi\mu_{\epsilon l}=W_{\epsilon l}(f,P)/W_{\epsilon l}(g,P)\,, \tag{2.11a}$$

where the Wronskians are evaluated at any radius $r\geq r_0$. FTD[1] emphasized instead the calculation of quantum defects by the phase-amplitude method (PAM). This method may be regarded as extending Eq. (2.11a) to the range $r\leq r_0$ allowing $\mu_{\epsilon l}$ to be a function of r in this range, and such that

$$\mu_{\epsilon l}=\lim_{r\to r_0}\mu_{\epsilon l}(r)\,. \tag{2.12}$$

In the PAM formulation $\mu_{\epsilon l}$ is generated by the potential difference $V_0(r')-V(r')$ over the range $0\leq r'\leq r$, by solving the nonlinear integral equation [Eq. (6) of FTD]

$$\pi\mu_{\epsilon l}(r)=\frac{2}{W(f,g)}\int_0^r dr'[V_0(r')-V(r')]\times[f(r')\cos\pi\mu_{\epsilon l}(r')-g(r')\sin\pi\mu_{\epsilon l}(r')]^2\,. \tag{2.13}$$

FTD noted that $\mu_{\epsilon l}$ often increases in rapid steps of magnitude close to unity; a main purpose of Sec. III will be to unravel the mechanism responsible for these rapid jumps in $\mu_{\epsilon l}$.

Thus far we have described only the most standard quantum defect $\mu_{\epsilon l}$, referred to the energy-normalized base pair (f,g). It is also possible, of course, to define alternative quantum defects by phase matching to different base pairs of solutions. In calculating the quantum defect one should probably use different base pairs in different energy ranges, so that the calculated quantity would have a minimal energy dependence. For example the energy-normalized base pair (f,g) used to define $\mu_{\epsilon l}$ in Eq. (2.10) is convenient because the bound state and normalization conditions in Eqs. (2.8) and (2.9) take such a simple form, and because at positive energies the short-range contribution to the scattering matrix is simply

$$S=e^{2i\pi\mu_{\epsilon l}}\,. \tag{2.14}$$

On the other hand, complications arise from the nonanalytic energy dependence of $\mu_{\epsilon l}$, particularly near $\epsilon=0$. When the long-range potential $V_0(r)$ is Coulombic, the nonanalyticity causes no serious difficulty, since $\mu_{\epsilon l}$ remains smooth at threshold. But for zero field, $\mu_{\epsilon l}$ obeys the Wigner threshold law $\mu_{\epsilon l}\propto k^{2l+1}$ as $k\to 0$, and even more seriously for the dipole potential $\mu_{\epsilon l}$ diverges as $\ln k$ as $k\to 0$. Thus the energy-normalized quantum defect $\mu_{\epsilon l}$ generally has an energy dependence which should be removed in the spirit of obtaining "smooth" quantities in the QDT. Another problem with the quantum defect $\mu_{\epsilon l}$ for the (f,g) basis arises for a Coulomb field only. Namely, when ϵ falls below the lowest Coulomb eigenvalue at $\nu=l$, the Coulomb eigenvalue at $\nu = 1$, the Coulomb functions (f,g) become imaginary and the quantum defect assumes an unphysical energy dependence. As discussed in I, quantum defects referred instead to (f^0,g^0), i.e., defined by

$$\tan\pi\mu^0_{\epsilon l} = W_{\epsilon l}(f^0, P)/W_{\epsilon l}(g^0, P)\,, \tag{2.11b}$$

are free from these anomalies. For the asymptotic Coulomb field, $\mu^0_{\epsilon l}$ is the same quantum defect which was denoted ξ in Ref. 9, whereas for zero field $(\tan\pi\mu^0_{\epsilon l})_{\epsilon=0}$ is the negative of the conventional scattering length. A third quantum defect will be useful in later sections for analysis at energies far below threshold and is referred to the base pair (f^+,f^-),

$$\tan\pi\mu^+_{\epsilon l} = W_{\epsilon l}(f^+, P)/W_{\epsilon l}(f^-, P)\,. \tag{2.11c}$$

III. GENERAL PROPERTIES OF PHASE-AMPLITUDE-METHOD PHASE SHIFTS

While the spectral behavior of quantum defects depends strongly on the potential several fundamental classes of behavior occur irrespective of the specific atomic fields. This circumstance allows us to illustrate the dominant features of $\mu^0_{\epsilon 0}(r)$ with a prototype—the $l = 0$ square well. This square well is shown in Fig. 1, with four regions in energy (I–IV) which exhibit qualitatively distinct properties:

(i) In region I both $P(r)$ and the pair (f^0,g^0) oscillate with wavelengths that approach each other in the limit $\epsilon \to \infty$, where $\delta_l \to 0$;

(ii) Region II covers a narrow energy range about $\epsilon = 0$ within which the nodal structure of $P(r)$ and (f^0,g^0) changes very little for $r < r_0$, allowing us to relate high-lying bound states to low-energy scattering phase shifts;

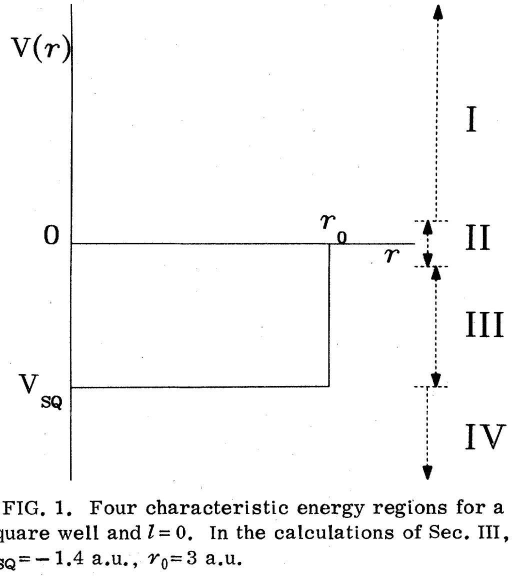

FIG. 1. Four characteristic energy regions for a square well and $l = 0$. In the calculations of Sec. III, $V_{SQ} = -1.4$ a.u., $r_0 = 3$ a.u.

(iii) In region III $P(r)$ still has radial oscillations while (f^0,g^0) begin their exponential growth within $r < r_0$, which induces an interesting stair-step dependence of $\mu^0_{\epsilon l}(r)$ on ϵ and on r;

(iv) In region IV both $P(r)$ and (f^0,g) are nodeless and rise exponentially at all $r \gtrsim |2\epsilon|^{-1/2}$, causing a monotonic energy dependence of $\mu^0_{\epsilon l}$.

The remainder of this section illustrates each class of quantum defect behavior explicitly and delineates the underlying mechanisms.

Evaluation of $\mu^0_{\epsilon 0}$ requires the regular solution $P(\epsilon, 0, r)$ of Eq. (2.1) for the square well, and also the zero-field analytic base pair (f^0,g^0). These radial wave functions were given in Eqs. (2.73) and (2.74) of I. [Actually (f,g) were given in I; we also use the relation $f^0 = k^{-l-1/2} f$, $g^0 = k^{l+1/2} g$.] These functions are

$$f^0(\epsilon, l=0, r) = \begin{cases} (2/\pi k^2)^{1/2} \sin kr, & \epsilon > 0 \\ (2\nu^2/\pi)^{1/2} \sinh(r/\nu), & \epsilon < 0 \end{cases}, \tag{3.1}$$

$$g^0(\epsilon, l=0, r) = \begin{cases} -(2/\pi)^{1/2} \cos kr, & \epsilon > 0 \\ -(2/\pi)^{1/2} \cosh(r/\nu), & \epsilon < 0 \end{cases},$$

where $2\epsilon = k^2 = -1/\nu^2$. The unnormalized radial solution of Eq. (2.1) for this optical potential is

$$P(\epsilon, l=0, r) = \begin{cases} \sin \bar{k} r, & \epsilon > V_{SQ},\ r < r_0 \\ \sinh(r/\bar{\nu}), & \epsilon < V_{SQ},\ r < r_0 \end{cases}, \tag{3.2}$$

where $2(\epsilon - V_{SQ}) = \bar{k}^2 = -1/\bar{\nu}^2$. The quantum defects in this optical potential can now be evaluated, giving for $r \leqslant r_0$,

$$\tan\pi\mu^0_{\epsilon 0}(r) = \begin{cases} \dfrac{\bar{k}\tan kr - k\tan\bar{k}r}{-\bar{k}k - k^2\tan kr\tan\bar{k}r}, & \epsilon > 0 \\[2ex] \dfrac{\bar{k}\nu^2\tanh(r/\nu) - \nu\tan\bar{k}r}{-\bar{k}\nu + \tanh(r/\nu)\tan\bar{k}r}, & 0 > \epsilon > V_{SQ}\,. \\[2ex] \dfrac{\nu^2\tanh(r/\nu) - \nu\bar{\nu}\tanh(r/\bar{\nu})}{-\nu + \bar{\nu}\tanh(r/\nu)\tanh(r/\bar{\nu})}, & \epsilon < V_{SQ}\,. \end{cases} \tag{3.3}$$

A. Phase-shift variations with energy

The energy dependence of $\mu^0_{\epsilon 0} \equiv \mu^0_{\epsilon 0}(r_0)$ over the entire spectrum of interest is shown in Fig. 2 for a square well that possesses two bound states. Although $\mu^0_{\epsilon 0}$ is plotted continuously below threshold the only physically relevant energies are those of the bound levels. These levels occur at intersections of the dashed curves

$$b^0_n(\nu) = n - \pi^{-1}\tan^{-1}(\nu)$$

with the full curve $\mu^0_{\epsilon 0}$. Atomic fields with an as-

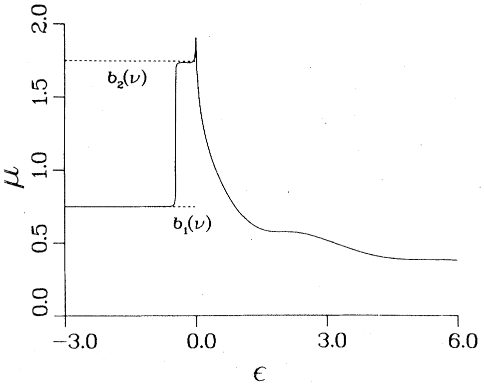

FIG. 3. "Energy-normalized" quantum defect at $r=r_0$ vs energy for the square well of Fig. 1. Discrete levels lie at intersections of dashed curves $b_n(\nu) = n - \frac{1}{4}$ with $\mu_{\epsilon 0}$.

ymptotic potential $V_0(r)=0$ possess at most one bound state in region II, since V_0 alone cannot bind a particle. In the example of Fig. 2 this region is a band of width $\Delta\epsilon \sim r_0^{-2} = \frac{1}{9}$ centered on $\epsilon = 0$. The higher of the two bound states occurs near the lower end of this range at $\epsilon_2 = -0.064$. Below this energy, region-III behavior sets in, which is *always* characterized by an extreme tendency for $\mu^0_{\epsilon l}$ to cling to the dashed curve that identifies bound states. This tendency arises, as described below, because (f^0, g^0) are both rising exponentially within the well $r < r_0$. Note the presence of one remarkable exception to this behavior though: at $\epsilon \sim -0.5$ a.u. the quantum defect rapidly changes from one bound-state curve to an adjacent one. This step in $\mu^0_{\epsilon 0}$ is in general associated with the occurrence of a region-III bound state. In region IV, $\mu^0_{\epsilon 0}$ clings to a single curve as there are no bound states as $\epsilon \to -\infty$. The opposite limit of large positive ϵ in region I is characterized by a general decrease of $\mu^0_{\epsilon 0}$ with ϵ, but modulated by weak shape resonance-type ringing induced by the sharp potential cutoff at r_0.

Thus far our discussion has focused on the analytic quantum defect $\mu^0_{\epsilon 0}$. But the phase shift usually discussed in scattering theory is instead the energy normalized one, $\pi\mu_{\epsilon 0}$, which is related to $\mu^0_{\epsilon 0}$ by

$$\tan\pi\mu_{\epsilon 0} = |2\epsilon|^{1/2}\tan\pi\mu^0_{\epsilon 0}, \tag{3.4}$$

for our square well. Application of this transformation to Fig. 2 leads to the energy-normalized quantum defect plotted in Fig. 3. [The dashed curves $b^0_n(\nu)$ of Fig. 2 are also transformed by Eq. (3.4), giving the curves $b_n(\nu)$ shown.] The familiar Wigner cusp dominates the behavior of $\mu_{\epsilon 0}$ in region II. The upward point of the cusp signifies the presence of at least one bound state, with the highest-lying bound state in region II or at the upper end of region III. This follows from Levinson's theorem,[10] which states that if $\mu_{\epsilon 0} = N$ at $\epsilon = 0$, there are N bound levels. Conversely a downward cusp signifies that no bound state occurs in region II; the sharper this cusp the closer the potential is to supporting an additional bound level. The behavior of $\mu_{\epsilon 0}$ in regions III and IV is quite similar to that of $\mu^0_{\epsilon 0}$ except that the bound-state curve $b_n(\nu)$, to which $\mu_{\epsilon 0}$ clings, has a form different from $b^0_n(\nu)$. We conclude that near threshold it is important to calculate the smooth $\mu^0_{\epsilon 0}$ instead of $\mu_{\epsilon 0}$. The high-energy ringing of $\mu_{\epsilon 0}$ in region I is smoother than that of the $\mu^0_{\epsilon 0}$ curve for energies $\epsilon \gtrsim 1$ a.u. In this region it appears then that $\mu_{\epsilon 0}$ is the preferred quantity to calculate, because of the more symmetric large-k

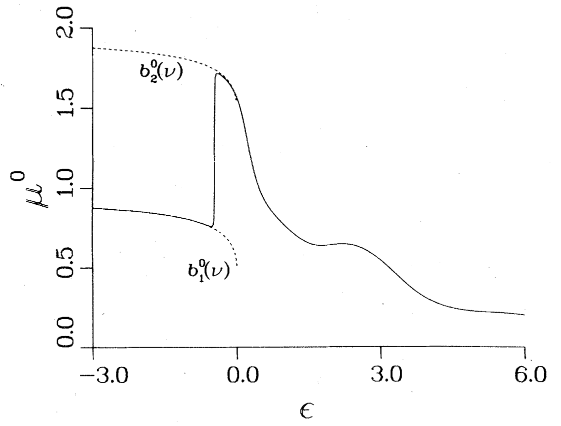

FIG. 2. "Analytic" quantum defect at $r=r_0$ vs energy (in a.u.), for the square well of Fig. 1 and $l=0$. Discrete levels lie at intersections of dashed curves $b^0_n(\nu)$ with $\mu^0_{\epsilon 0}$. The sharp step of μ^0 is discussed in the text.

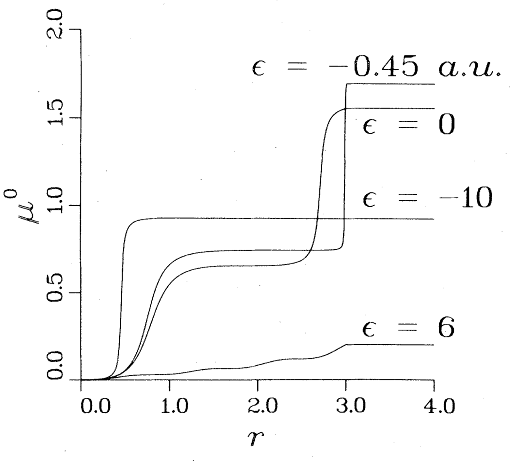

FIG. 4. "Analytic" quantum defect vs radius (in a.u.) for the square well, $l=0$ and for energies in the four regions I–IV of Fig. 1.

forms of (f,g) given in Eq. (2.5a). Section IV discusses further the relative usefulness of $\mu_{\epsilon l}$ and $\mu^0_{\epsilon l}$ for realistic atomic fields.

B. Phase-shift variations with radius

The analysis of the energy dependence of $\mu^0_{\epsilon 0}(r_0)$ can be extended into a mapping of the two-variable function $\mu^0_{\epsilon 0}(r)$, defined by Eq. (2.11b), as a surface over the coordinate plane (ϵ, r). But before studying the joint variations simultaneously, first consider the several slices of this surface at constant ϵ plotted in Fig. 4. In region I ($\epsilon = 6$ a.u.) $\mu^0_{\epsilon 0}(r)$ increases smoothly toward its limiting value at r_0, whereas in region II ($\epsilon \sim 0$) it rises in a definite stair-step fashion. The stair-step pattern of phase-shift accumulation is sharpened in region III ($\epsilon = -0.45$), with an extremely rapid second step at $r \sim 2.9$. This latter step is absent in region IV ($\epsilon = -10$), but a single radial step persists even as $\epsilon \to -\infty$.

Two quantities dictate the form of the radial phaseshift accumulation: (i) the relative wavelengths of oscillation of $P(r)$ and $f^0(r)$ which are dictated by the local kinetic energies,

$$T(r) \equiv \tfrac{1}{2} k_P^2(r) = \epsilon - V(r) - l(l+1)/2r^2\,,$$
$$T_0(r) \equiv \tfrac{1}{2} k_f^2(r) = \epsilon - V_0(r) - l(l+1)/2r^2\,, \tag{3.5}$$

and (ii) the ratio of the amplitudes of the base-pair wave functions, $|f^0/g^0|$.

The importance of (i) can be best assessed by using a WKB approximation for $P(r)$ and (f,g) to evaluate the Wronskians in Eq. (2.11a). After some rearrangement, this approximation to $\mu_{\epsilon l}(r)$ reduces to

$$\pi \mu^{\mathrm{WKB}}_{\epsilon l}(r) = \phi_P(r) - \phi_f(r)\,, \tag{3.6}$$

where

$$\phi_P(r) = \tan^{-1}\left[\frac{k_f(r)}{k_P(r)} \tan\left(\int_{r_{\mathrm{I}}}^{r} dr'\, k_P(r')\right)\right],$$
$$\phi_f(r) = \int_{r_{\mathrm{I0}}}^{r} dr'\, k_f(r')\,, \tag{3.7}$$

and where r_I and r_{I0} are the inner classical turning points for motion in the two potentials $V(r)$ and $V_0(r)$. We interpret $\phi_P(r)$ and $\phi_f(r)$ as the phase functions of $P(r)$ and $f(r)$. The presence of $k_f(r)$ in the expression for $\phi_P(r)$ ensures that oscillations of $P(r)$ are measured in units of the wavelength of $f(r)$. The expressions (3.6) and (3.7) are exact above threshold for the present square-well example, and the integrals in (3.7) are linear in r since $k_P = \bar{k}$ and $k_f = k$. We see that $\phi_f(r)$ increases smoothly with r, but the accumulation of $\phi_P(r)$ varies qualitatively with the energy. Far above threshold $\phi_P \approx \bar{k} r$ and $\pi \mu_{\epsilon l}$ increases linearly in r, as in the $\epsilon = 6$ a.u. curve of Fig. 4. Near threshold, conversely, the ratio $k_f/k_P = k/\bar{k}$ is very small, keeping ϕ_P close to a multiple of π except where $\bar{k} r \approx (n + \frac{1}{2})\pi$. At these radii ϕ_P rises by $\sim\pi$ quite rapidly, causing in turn a unit step in $\mu_{\epsilon 0}(r)$.

While the variations of the wave number ratio k_f/k_P have explained the different phase-shift behavior in regions I and II, the factor $|f^0/g^0|$ can also act to sharpen the stair-step character. This is most clearly demonstrated by rearranging Eq. (2.11b) in the form

$$\tan \pi \mu^0_{\epsilon 0} = \frac{(P'/P) - (f^{0\prime}/f^0)}{(P'/P) - (g^{0\prime}/g^0)}\, \frac{f^0}{g^0}\,. \tag{3.8}$$

In those regions of ϵ and r where the ratio f^0/g^0 is small, $\tan \pi \mu^0_{\epsilon 0}$ tends to remain quite small too. But very near those "step radii" where the denominator of Eq. (3.8) vanishes, $\mu^0_{\epsilon 0}(r)$ rises rapidly by unity. This occurs whenever $P(\epsilon, l, r)$ oscillates at small $r \ll |2\epsilon|^{-1/2}$ because at small radii (f^0/g^0) is roughly r^{2l+1}. This leads to exceedingly fast steps in $\mu^0_{\epsilon l}(r)$ in the inner shells of heavy atoms; for example the 3d antinode of uranium is at $r \sim 0.1$, where $r^{2l+1} = 10^{-5}$.

A similar dependence of $\mu^0_{\epsilon l}$ on r is observed in the opposite extreme, when an antinode of $P(r)$ occurs at large $r \gg \nu$. In that case, however, $|f^0/g^0| = O(1)$, since both f^0 and g^0 are proportional to $e^{r/\nu}$. In this extreme then, it is more appropriate to consider $\mu^+_{\epsilon l}(r)$, noting that $|f^+/f^-| = O(e^{-2r/\nu})$. Region III is characterized by having $T(r) > 0$ but $T_0(r) < 0$. In general in this region, $\mu^+_{\epsilon l}(r)$ clings to integer values within an exponentially small number, though at certain radii $\mu^+_{\epsilon l}(r)$ increases from one integer n to $n+1$. Evaluation of $\mu^+_{\epsilon 0}(r)$ for the s-wave square well shows this explicitly:

$$\tan \pi \mu^+_{\epsilon 0}(r) = \begin{cases} \dfrac{\bar{k}\nu + \tan \bar{k} r}{\bar{k}\nu - \tan \bar{k} r}\, e^{-2r/\nu}, & 0 > \epsilon > V \\[2ex] \dfrac{\nu + \bar{\nu} \tanh(r/\bar{\nu})}{\nu - \bar{\nu} \tanh(r/\bar{\nu})}\, e^{-2r/\nu}, & V > \epsilon\,. \end{cases} \tag{3.9}$$

Owing to the exponentially small factors, $\mu^+_{\epsilon 0}(r)$ will be dominated by its tendency to remain an integer throughout regions III and IV, both as a function of r and of ϵ, with the exception of a small number of rapid steps. These properties of $\mu^+_{\epsilon 0}(r_0)$ are illustrated in Fig. 5 for the $l = 0$ square well. The constancy of $\mu^+_{\epsilon 0}$ is prominent for all $\nu \lesssim 2$ owing to the decaying exponential factor in Eq. (3.9). This simple behavior of $\mu^+_{\epsilon 0}$ in regions III and IV is in turn responsible for the clinging of $\mu^0_{\epsilon 0}(r_0)$ to the curves $b^0_n(\nu)$ in Fig. 2. While both

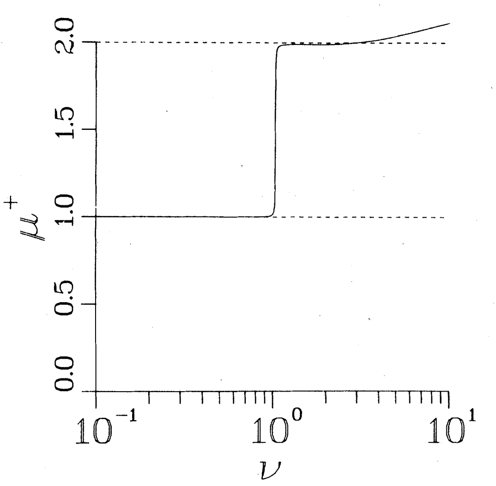

FIG. 5. Quantum defect μ^+ vs effective quantum number $\nu = (-2\epsilon)^{-1/2}$ for the square well and $l = 0$. This parameter clings to integer values in regions III and IV.

$\mu^0_{\epsilon l}$ and $\mu_{\epsilon l}$ can assume a more complicated energy dependence in regions III and IV for different long-range fields, the quantum defect $\mu^+_{\epsilon l}$ is always very nearly an integer. Regardless of the long-range potential however, a good representation of the quantum defect far below threshold is always

$$\tan \mu^+_{\epsilon l}(r) \xrightarrow[r/\nu \gg 1]{} \frac{(P'/P) + 1/\nu}{(P'/P) - 1/\nu} e^{-2r/\nu} r^{2\xi}, \qquad (3.9')$$

which follows from Eqs. (2.46) and (2.11c). [The general relation between $\mu^+_{\epsilon l}$ and $\mu^0_{\epsilon l}$ is given in Eq. (4.3).] In the limit of $\nu \to 0$ in region IV, $P'/P \sim 1/\bar{\nu}$, showing not only that $\mu^+_{\epsilon l}$ is very nearly an integer, but also that it is *less* than an integer. This is generally true in region IV, provided $V(r) < V_0(r)$ at all r.

It is important to note that the condition for a bound state takes a very simple form in terms of $\mu^+_{\epsilon l}(r_0)$ *irrespective of the form of the long-range potential*, namely,

$$\mu^+_{\epsilon_n l}(r_0) \text{ is an integer}, \qquad (3.10)$$

as required for $P(\epsilon_n, l, r)$ to be proportional to f^+ for $r > r_0$. The analytic quantum defect $\mu^0_{\epsilon l}$ is unambiguously specified in terms of $\mu^+_{\epsilon l}$, using the known linear transformation from (f^0, g^0) to (f^+, f^-) for the relevant long-range field. This transformation differs for the three alternative fields (zero, Coulomb, or dipole). Hence although $\mu^+_{\epsilon l}(r)$ clings to integer values far below threshold for any of these fields, $\mu^0_{\epsilon l}(r)$ will "cling" to a different curve $b^0_n(\nu)$ for each different field.

C. Phase-shift surfaces

To this point the analysis of $\mu^0_{\epsilon 0}(r)$ has dealt only with variations at fixed r or at fixed ϵ. A natural extension of this discussion is to plot $\mu^0_{\epsilon 0}(r)$ as a surface depending on (ϵ, r), showing more clearly the interplay of the energy and radius dependences. The negative and positive energy plots are shown in Fig. 6(a) and 6(b) for the square well we have discussed earlier. The far edge of the two surfaces ($r = 3$ a.u.) reproduces the energy dependence of $\mu^0_{\epsilon 0}(r_0)$ shown in Fig. 2. The (near-threshold) region II persists in Fig. 5(a) for $\nu \gtrsim 3$; here $\mu^0_{\epsilon 0}$ is roughly energy independent at all radii. The first notable feature occurs as ν decreases from threshold to $\nu \sim 1$, the energy at which $\mu^0_{\epsilon 0}(r_0)$ changes by very nearly 1. Over a narrow interval in ν, the second radial step of $\mu^0_{\epsilon 0}(r)$ begins to move slowly outward, and as this radial step moves outward the ratio $|f^+/f^-|$ becomes smaller. The smallness of this ratio in turn sharpens the radial step. [This is seen more clearly by comparing the second radial steps in $\mu^0_{\epsilon 0}(r)$ at $\epsilon = 0$ and $\epsilon = -0.45$ in Fig. 4.] Eventually, as ν decreases further the extremely rapid second radial step moves beyond the radius r_0, causing $\mu^0_{\epsilon 0}(r_0)$ to drop by unity quite suddenly. This interprets the rapid drop of $\mu^0_{\epsilon 0}$ in Fig. 2 in terms of a smoother radial progression which

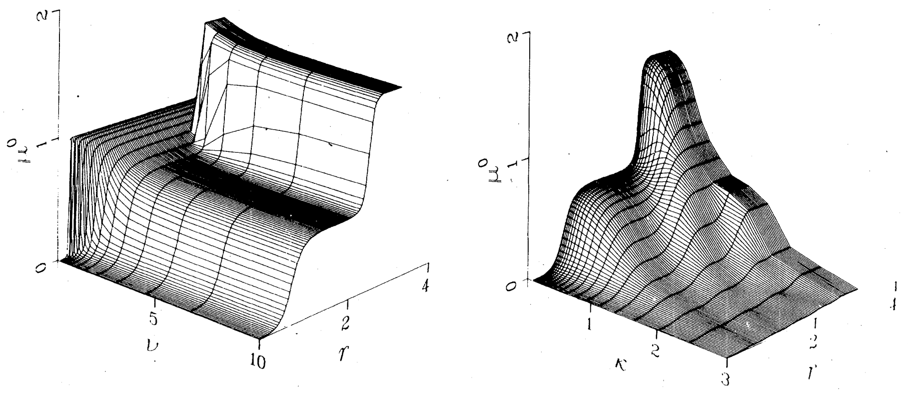

FIG. 6. "Analytic" quantum-defect surface for the square well of Fig. 1. (a) $\epsilon < 0$: μ^0 vs effective quantum number ν and radius r; (b) $\epsilon > 0$: μ^0 vs wave number k and r. The small-k edge of (b) joins smoothly to the large ν edge of (a).

would have been difficult to deduce from Fig. 2 alone. Interestingly, while the second radial step moves outward as ν is decreased, the first step moves inward. This is a quite general feature of the phase surface, as will be seen in Fig. 10 of Sec. IV A.

The positive-energy half of the surface is shown in Fig. 6(b). The $k=0$ edge connects smoothly to the $\nu=\infty$ edge of Fig. 6(a). The evolution of this surface as k increases is, not surprisingly, entirely different from the negative-energy surface. In accordance with Fig. 2 there are no sudden steps of $\mu^0_{\epsilon 0}(r_0)$; rather the surface slowly diminishes in height as k increases. There remain to be explained two "ripples" which are present on the surface between $k=0.8$ and $k=2$. Recall two fundamental facts: (i) the radial nodes of all solutions $P(r)$ of Eq. (2.1) are decreasing functions of k; (ii) $d\mu^0_{\epsilon 0}(r)/dr$ vanishes at each radial node of $P(r)$. Thus the ripples are just the radial points of inflection, all of which move to smaller radii as k increases. These points of inflection can be seen more clearly in the $\epsilon=6$ a.u. plot of $\mu^0_{\epsilon 0}(r)$ in Fig. 4. The stair-step behavior of $\mu^0_{\epsilon 0}$ is diminished as k increases through region I where the Born approximation improves.

IV. APPLICATIONS

Next we use the analysis of the Sect. III to discuss two realistic problems, thus illustrating the applicability of the unified treatment of Sec. III to quite diverse phenomena.

A. Atomic quantum defects

The emphasis thus far has been on regularities which persist irrespective of the details of the potential. This emphasis will be altered now as we focus less on the systematics and more on the individual variations, the true fingerprints of the system's dynamics. Calculated quantum defects for orbital momenta $l=0$, 1, and 2 of neutral potassium are shown at $\epsilon<0$ in Figs. 7(a)–9(a), and at $\epsilon>0$ in Figs. 7(b)–9(b). The calculation consisted of first solving Eq. (2.1) for $P(\epsilon, l, r)$ via Numerov's method,[11] using the Herman-Skillman[12] atomic potential as $V(r)$, and then applying Eq. (2.11b) to determine $\mu^0_{\epsilon l}(r)$. The energy dependence of each of these partial-wave phase shifts resembles the square-well results of Fig. 2, though a number of important differences are present.

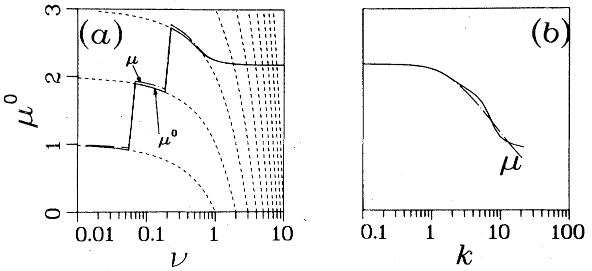

FIG. 7. Analytic (——) and energy normalized (–·–) quantum defects at $r=r_0$ for potassium with $l=0$: (a) versus effective quantum number ν; discrete levels lie at intersections of the dashed curves $b^0_n(\nu)$ with μ^0; (b) versus wave number k; this figure joins smoothly to (a) at zero energy, where μ and μ^0 are equal.

In Figs. 7(a)–9(a) the dashed curves represent the function $b^0_n(\nu)$ whose intersections with the full curve $\mu^0_{\epsilon l}(r_0)$ determine the bound-state energies, as in Fig. 2. Here, however, $b^0_n \sim n-\nu$ at large ν in correspondence with the long-range unit-charge Coulomb potential experienced by the outer electron, thus generating the infinite number of Rydberg levels. More specifically,

$$b^0_n(\nu)=n-\pi^{-1}\cot^{-1}(A\cot\pi\nu+\mathcal{G}) \tag{4.1}$$

where $\epsilon=-1/2\nu^2$, and where the energy-dependent parameters A and $\mathcal{G}$ are given in Table I of I. Also shown in Figs. 7(a)–9(a) (for $\nu>l$ only) is the energy normalized quantum defect $\mu_{\epsilon l}$ whose plot is represented by a dash-dotted curve. We see that $\mu^0_{\epsilon l}$ varies somewhat more slowly than $\mu_{\epsilon l}$ near and far below threshold, but Figs. 7(b)–9(b) show $\mu_{\epsilon l}$ to become smoother as ϵ rises to large positive values. This appears to settle the controversy in the quantum-defect-theory literature[9] over which of $\mu_{\epsilon l}$ or $\mu^0_{\epsilon l}$ can be calculated on a coarser mesh: $\mu^0_{\epsilon l}$ is to be calculated near and below and $\mu_{\epsilon l}$ far above threshold.

The dependence of $\mu_{\epsilon l}(r_0)$ on l can be understood rather simply, using qualitative estimates for the phase parameters $\phi_p(r_0)$ and $\phi_f(r_0)$ of Eq. (3.6). At $\epsilon=0$ for example, the atomic wave function $P(r)$ has either n_l-l-1 or n_l-l nodes inside $r<r_0$, where n_l is the principal quantum number of the lowest unoccupied orbital with a given l (e.g., $n_0=4$ for K). Accordingly $\phi_p(r_0)$ at $\epsilon=0$

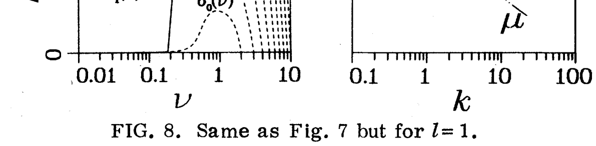

FIG. 8. Same as Fig. 7 but for $l=1$.

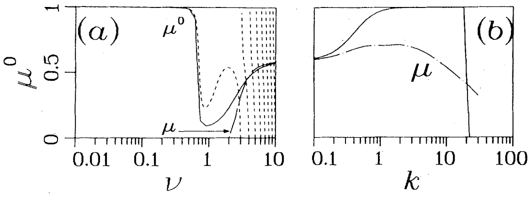

FIG. 9. Same as Fig. 7 but for $l=2$.

must lie in the interval

$$n_l - l - 1 < \phi_P(r_0)/\pi < n_l - l\,. \tag{4.2}$$

For a rough estimate we use the intermediate value $\phi_P(r_0) \sim \pi(n_l - l - \frac{1}{2})$. To estimate the Coulomb phase function we note that at $\epsilon = 0$, $f^0(r)$ has one node inside r_0 at $l=0$ for nearly all atoms, and no nodes inside r_0 for higher l ($r_0 \sim 3$ for potassium). Thus $\phi_f(r_0) \sim \pi$ for $l=0$, $\phi_f(r_0) \sim 0$ for $l>0$. These considerations alone yield the following crude estimates of μ_{0l}: 2.5, 2.5, and 0.5 for $l = 0$, 1, and 2. These can be compared with the more accurate calculated and experimental values in Table I; the large error in these rough estimates arises largely from the crude guess for $\phi_f(r)$. A more realistic approach is to use the large-r form of the exact zero-energy Coulomb-field solution $f = r^{1/2} J_{2l+1}(\sqrt{8zr}\,)$ for calculating

$$\cot\phi_f = k_f^{-1}(r_0) f'(r_0)/f(r_0)\,.$$

This procedure leads to estimates $\phi_f/\pi \sim 1.3$, 0.5, and 0 for $l=0$, 1, and 2, changing our respective estimates of μ_{0l} to 2.2, 2.0, and 0.5, which are much better but still far from exact. Table I also gives an indication of the validity of the Hartree-Slater[12] approximation to the atomic field. Namely, the $l=0$ and $l=1$ calculated quantum defects are very close to the experimental values, but $\mu_{02}(r_0)$ shows a large discrepancy. This discrepancy results from the delicate balance between centrifugal and electrostatic forces which is strongly model dependent for $l=2$.

The regular spacing of Rydberg levels hinges on the slow variation of $\mu^0_{\epsilon l}(r_0)$ as a function of energy throughout region II of the spectrum. This regularity breaks down near the lower end of the series, reflecting the transition from region II to region III. As emphasized in Sec. III, the onset of region III occurs when the base-pair functions (f^0, g^0) begin their exponential growth within the core $r < r_0$ (say, when $r_0 \gtrsim 2\nu$). In this range it is the alternative quantum defect $\mu^+_{\epsilon l}$ which becomes nearly constant. According to Eq. (3.9′) $\mu^+_{\epsilon l}$ is an integer to within an exponentially small difference [of order $e^{-2r_0/\nu}$, except for energies at which $P'(r_0)/P(r_0) - 1/\nu = O(\nu/r_0)$]. As ϵ is decreased through this range, $\mu^+_{\epsilon l}$ drops rapidly to the lower adjacent integer. A bound level then occurs where $\mu^+_{\epsilon l}$ is exactly integer; that is, the numerator of (3.9′) vanishes. At the energies where $\mu^+_{\epsilon l}$ rapidly drops, the analytic quantum defect $\mu^0_{\epsilon l}$ also makes a transition from one of the dashed curves of Fig. 7(a) or 8(a) to the next one according to the relationship

$$\tan\pi\mu^0_{\epsilon l} = \frac{D^2 \tan\pi\mu^+_{\epsilon l} - \tan\beta_l}{A(1 + D^2 \tan\beta_l \tan\pi\mu^+_{\epsilon l}) + \mathcal{G}(\tan\beta_l - D^2\tan\pi\mu^+_{\epsilon l})} \tag{4.3}$$

which follows from Eqs. (2.5b), (2.7), and (2.11a). No rapid steps of $\mu^0_{\epsilon l}$ occur in Fig. 9(a) because there are no $l=2$ core electrons; thus region III is so narrow that it can be disregarded for this value of l. The Rydberg series terminates at the threshold of region III of the spectrum because each of the levels below this threshold is occupied by a core electron. (The wave functions of these core electrons decay exponentially for $r \gtrsim r_0$ and are in fact disregarded here for all $r > r_0$.)

Throughout regions III and IV $\mu^+_{\epsilon l}$ remains slightly *less than* (but extremely close to) a positive integer, except near the rapid jumps. Equation (4.3) then requires $\mu^0_{\epsilon l}$ to lie just below the corresponding dashed curve in each of Figs. 7(a)–9(a). These dashed curves $b^0_n(\nu)$ defined by Eq. (4.1) are sensitive functions of l in the energy range $\nu < l$, where they assume a nonmonotonic energy dependence.[13] In the limit $\nu \to 0$ at the lower end of region IV, note that $\mu^0_{\epsilon l}$ approaches 0 for odd l and unity for even l. This is determined by the explicit low-ν form of Eq. (4.1)

$$b^0_n(\nu) \xrightarrow[\nu\to 0]{} n + (-1)^{l+1} \nu^{2l+1} 2\pi/(l\,!)^2\,. \tag{4.4}$$

Only those curves $b^0_n(\nu)$ which are positive are relevant, since the quantum defect is positive by Eq. (2.13). Thus, the lowest positive curve near $\nu \sim 0$ approaches 0 for odd l and unity for even l.

The Rydberg series terminates at different energies for different atoms. This is illustrated by the quantum defects of sodium, aluminum,

TABLE I. Experimental (Ref. 14) and calculated potassium quantum defects.

	$\mu_{\epsilon=0,\,l}(r_0)$	
l	Hartree Slater	Experimental
0	2.178	2.178
1	1.712	1.701
2	0.590	0.278

phosphorus, and potassium shown in Fig. 10 for $\epsilon < 0$. One notes first in Fig. 10 that $\mu_{\epsilon 0}$ increases with Z at all ϵ, which reflects the increasing attraction of the atomic potential. For each of these atoms $\mu_{\epsilon 0}$ varies slowly at large ν until ν decreases below the lowest Rydberg level in the transition region $1<\nu<3$. At the onset of region III the Na quantum defect converges to the dashed curve $b_2(\nu)=2-\nu$, while it converges to $b_3(\nu)=3-\nu$ for the three higher-Z atoms shown. This abrupt change from one dashed curve to the next as Z increases from 11 to 13 reflects the abrupt increase in the size of the ion core as its $n=3$ shell starts filling. More specifically, the alkali-metal-like core of Mg ($Z=12$) extends roughly 1 a.u. beyond the closed-shell core of Na: in the Hartree-Slater model $r_0=3.2$ for Mg but only 2.2 a.u. for Na. Since the onset of region III occurs at $\nu \sim r_0/2$, $\mu_{\epsilon 0}$ should converge to one of the dashed curves $b_n(\nu)$ at a *higher* energy for Mg than for Na. Accordingly we expect that this sudden change from the lower dashed curve ($n=2$) to the upper dashed curve ($n=3$) occurs first for the Mg quantum defect (which was not calculated in this study). A similar transition should also take place at each alkaline-earth element.

The earlier onset of region III for the alkaline-earth elements implies that they have a more negative derivative $d\mu_{\epsilon 0}/d\epsilon$ than the alkali metals. The Z dependence of this derivative at $\epsilon=0$, plotted in Fig. 9 of FTD,[1] shows explicitly that $|d\mu_{00}/d\epsilon|$ is roughly twice as large for each group-II element than for the adjacent group-I element. Thus the non-Coulomb contribution to Wigner's time-delay index $2\pi\, d\mu_{\epsilon 0}/d\epsilon$, is more negative for Mg than Na. This is physically reasonable, since a low-energy electron experiences an acceleration throughout a much larger volume and so emerges from the core sooner when scattered by Mg^+ than when scattered by Na^+.

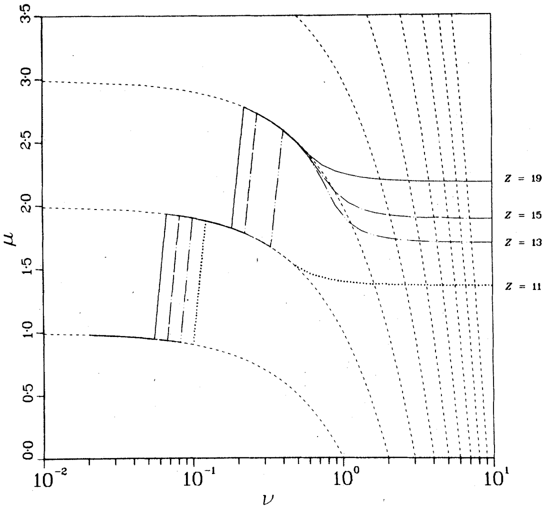

FIG. 10. Energy normalized quantum defect for $l=0$, at $r=r_0$ vs ν for sodium (• • • •), aluminum (—• • —), phosphorus (— — • — —), and potassium (——). Dashed curves represent $b_n(\nu)=n-\nu$ and bound levels as in Fig. 3.

1. Joint variations with ϵ and r

The potassium phase-shift surfaces are shown in Figs. 11(a)–11(c) at $\epsilon<0$ and for $l=0$, 1, and 2, respectively. The positive-energy surfaces are not shown here as they are quite similar to the square-well surfaces of Fig. 6(b). We can learn about the atomic dynamics, however, from the negative-energy surfaces. Near threshold, at the right-hand edge of Fig. 11(a), the quantum defect increases in a stair-step fashion. Note that the step spacings increase while successive step heights decrease as r increases. This differs from the phase-shift accumulation for the square well (see Fig. 4), where the $\epsilon=0$ quantum defect increased in a stepwise fashion throughout $r<r_0$. The atomic problem differs from the square well in this respect because the potential difference $V_0(r)-V(r)$, which determines $d\mu^0_{\epsilon l}(r)/dr$ through Eq. (2.13), is not constant but instead decreases smoothly as r increases and vanishes at $r \geq r_0$. Accordingly the ratio $k_f(r)/k_P(r)$ in Eq. (3.7) goes to unity as $r \to r_0$. Since the atomic radial wave function $P(\epsilon, l, r)$ has an antinode centered on each subshell of a given l, the rapid steps of $\mu^0_{\epsilon l}(r)$ occur at these radii also. Thus the first jump occurs at the $1s$ subshell at $r \sim 0.05$ for $l=0$ and at the $2p$ subshell near $r \sim 0.19$ for $l=1$, while P has no antinodes within $r<r_0$ for $l \geq 2$. Much as in Fig. 6(a), a decrease of the energy below the Rydberg termination energy causes the outermost radial step to sharpen and to move outward (for $l=0$ and 1 only). When ϵ is decreased sufficiently this radial step moves "beyond" r_0, causing the rapid steps in the energy dependence of $\mu^0_{\epsilon l}(r_0)$ shown in Figs. 7(a) and 8(a). Because potassium has no levels bound in the *inner well* for $l \geq 2$, there are no similar steps of $\mu^0_{\epsilon l}(r_0)$ with energy. In the limit $\nu \to 0$ each radial curve has either one step or none, depending on the explicit form of the dashed curves $b^0_n(\nu)$ defined in Eq. (4.1).

B. H^- quantum defects

The preceding example emphasized the independent-electron model of atomic structure. To improve on that model it is necessary to explicitly treat the effect of electron correlations. One such approach, which treats the correlations nonper-

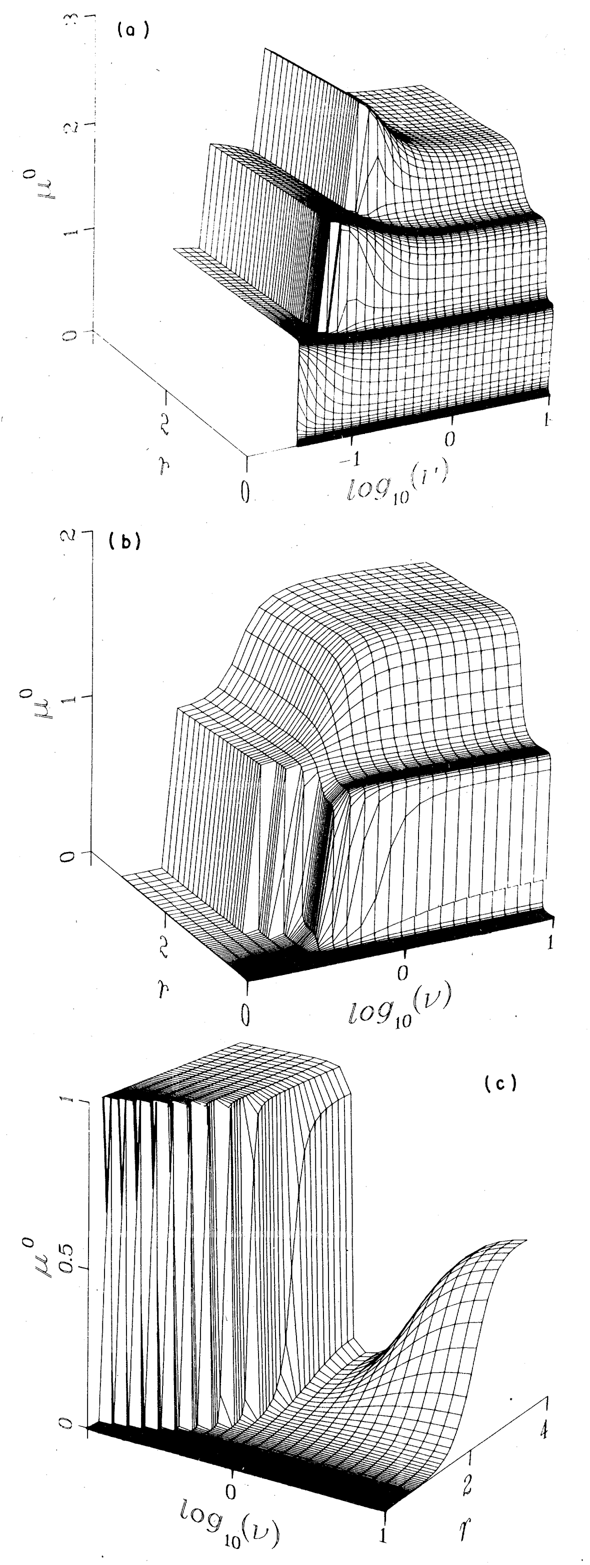

FIG. 11. Analytic quantum defect $\mu^0_{\epsilon l}(r)$ for potassium vs r and ν as in Fig. 6(a), but from a different perspective. (a) $l=0$, (b) $l=1$, (c) $l=2$.

turbatively, is the hyperspherical-coordinate method used by Macek, Lin, and Fano[5] to characterize doubly excited channels of He and H$^-$. Their studies demonstrated that the nonseparable two-particle Schrödinger equation in the variables r_1, θ_1, φ_1, r_2, θ_2, φ_2 can often be separated approximately, and thus reduced to an equation for motion in a local potential of the single variable

$$R=(r_1^2+r_2^2)^{1/2} .$$

Within this approximation we can apply a single-channel QDT treatment.

In addition to R one must consider five coordinates independent of R, which we label collectively as Ω. Macek expanded the wave function in a complete set of eigenfunctions $\Phi_\mu(R;\Omega)$ which diagonalize the Hamiltonian with R held fixed; we write this as

$$H_{R=\text{const}}\,\Phi_\mu(R;\Omega)=U_\mu(R)\Phi_\mu(R;\Omega)\ . \tag{4.5}$$

The eigenvalues $U_\mu(R)$ then act as adiabatic potential curves which smoothly connect the condensed ($R\rightarrow 0$) and dissociative ($R\rightarrow\infty$) limits, analogous to the united-atom and separated-atom limits of molecular physics. More specifically, Macek's expansion took the form

$$\psi=R^{-5/2}\sum_\mu \Phi_\mu(R;\Omega)P_\mu(R)\ , \tag{4.6}$$

where the factor $R^{-5/2}$ has been separated for convenience. Substitution of Eq. (4.6) into the two-electron Schrödinger equation, followed by multiplication by $\Phi_{\mu'}$ and integration over Ω, gives the infinite set of coupled hyperradial equations:

$$\left(\frac{d^2}{dR^2}+2E-2U_\mu(R)\right)P_\mu(R)+\sum_{\mu'}2W_{\mu\mu'}(R)P_{\mu'}(R)=0\ . \tag{4.7}$$

The coupling coefficients $W_{\mu\mu'}$ represent departures from the adiabatic approximation. Macek[5(a)] found that these off-diagonal couplings can often be neglected, thus reducing the electron correlation problem (4.7) to an effective one-dimensional Schrödinger equation. A *multichannel* QDT approach is then required when the $W_{\mu\mu'}$ are not negligible for $\mu\neq\mu'$, but here we have ignored these coupling terms.

This approach has been utilized recently by Lin[5(c)] to classify $^1P^o$ H$^-$ resonances near the $n=2$ threshold of H. The adiabatic-potential curves $U_\mu(R)$ he obtained (including also the diagonal element $W_{\mu\mu}$) are shown in Fig. 12. Note that at large R as one electron escapes from a hydrogen atom in its $n=2$ states, there is one attractive channel "$sp-$", and two repulsive channels "$sp+$" and "pd." Lin[5(c)] showed that the $sp+$ channel supports no bound states but does support a strong shape resonance just above the $n=2$ threshold. The pd channel is completely repulsive and plays no role in the excitation processes near threshold. The $sp-$ channel, though, is attractive at large R, where it is represented by

$$2U_{sp^-}(R) - 2W_{sp^-,sp^-} \xrightarrow[R\to\infty]{} -0.25 - 3.71/R^2 , \qquad (4.8)$$

in atomic units, disregarding spin-orbit coupling and the Lamb shift. This potential, generated by the dipole moment of a $2s$-$2p$ hybrid state of H, supports an infinite number of bound levels,[15] corresponding to the "dipole" type of long-range field of Eq. (2.2), with $a=1.86$. It is this channel which gives rise to the observed[16] and calculated[17] $^1P^o$ Feshbach resonances below the threshold, of which only the lowest one has been observed experimentally. Of course the states of this channel lie in the continuum of H(1s) + ϵp, but their coupling to this continuum amounts to only a weak perturbation $W_{1s\epsilon p,sp^-}$. Disregarding this perturbation permits us to discuss the level structure of the $sp-$ states by single channel QDT.

Using Lin's "$sp-$" potential curve it was straightforward to solve Eq. (4.7) for $P_{sp^-}(R)$ and to phase-match this function to the dipole-field base pair (f^0,g^0) defined in I (at $R=R_0\sim 25$ a.u.). According to the convention of Eq. (2.5) of I, the dipole-field solutions are given in terms of Bessel functions by

$$\begin{aligned}(\nu/\pi)^{1/2}D(\nu,a)f^+ &\\ &= -2(1-e^{-2\pi a})^{-1/2}r^{1/2}\,\mathrm{Im}[J_{ia}(ir/\nu)]\\ (\nu/\pi)^{1/2}D^{-1}(\nu,a)f^- &\\ &= 2(1-e^{-2\pi a})^{-1/2}r^{1/2}\,\mathrm{Re}[J_{ia}(ir/\nu)] ,\end{aligned} \qquad (4.9)$$

with $a=1.86$ as above. The base pair $(f,g) = (f^0,g^0)$ for the dipole field at negative energies, and is expressed by Eq. (2.5b) in terms of the functions in Eq. (4.9). These functions were determined numerically by using the series expansion for Bessel functions.[18] The solution of Eq. (4.7) was obtained as above in Sec. IV A, and Eq. (2.11a) then determined $\mu^0_{\epsilon a}$. The results of this calculation are plotted in Fig. 13. As in the earlier quantum-defect plots, the intersection of $\mu^0_{\epsilon a}$ with any of the dashed lines,

$$b^0_n(\nu) = n - \pi^{-1}a\ln 2\nu + \pi^{-1}\arg\Gamma(1-ia) ,$$

of Eq. (2.9) represents a physically observable bound state. Note that *all* bound states of the sp-channel occur in the near-threshold region II, throughout which $\mu^0_{\epsilon a}$ remains very nearly constant ($\mu^0_{\epsilon a}$ changes only by ~0.004 between $\epsilon=0$ and the lowest bound level at $\nu_1 \sim 22.45$, $\epsilon_1 \sim -0.001\,98$ Ry). Also, whereas a long-range Coulomb field has bound states whenever ν increases by unity, here the successive bound states converge geometrically to the condensation point, according to

$$\nu_{n+1} \sim \nu_n e^{\pi/a} = 5.4\,\nu_n .$$

(The binding energy of the lowest level of this series lies roughly 7×10^{-5} Ry lower than Lin's value[5(c)]; this 4% discrepancy probably results

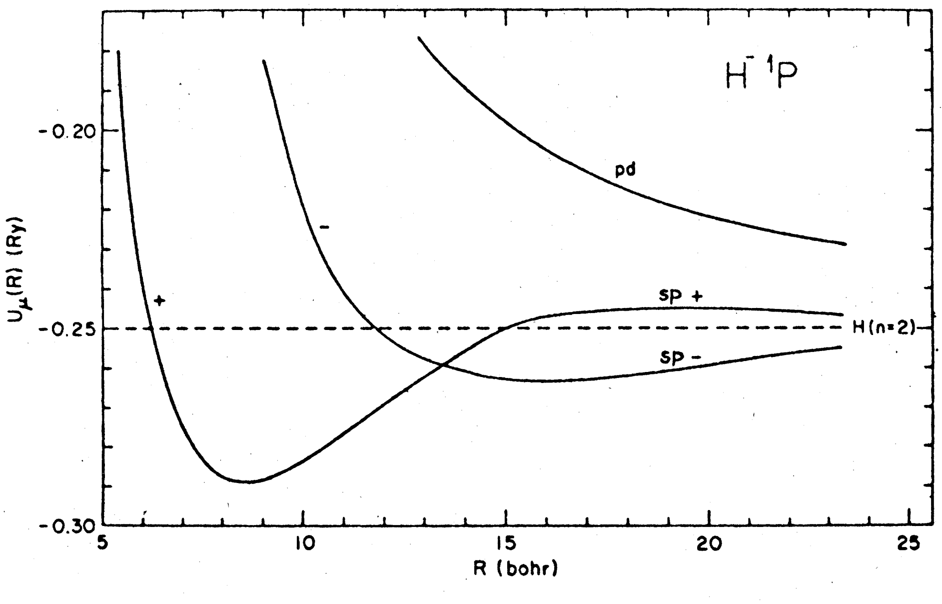

FIG. 12. Adiabatic-potential curves $U_\mu(R)$ of H$^-$ $^1P^o$ states that converge to the $n=2$ level of H [from Ref. 5(c)].

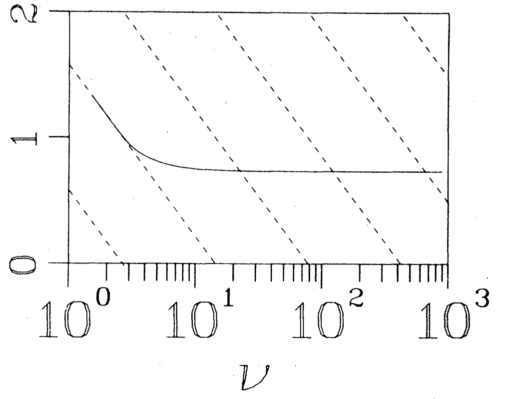

FIG. 13. Analytic quantum defect at $R=R_0$ for the "$sp-$" ${}^1P^0$ channel of H$^-$ vs effective quantum number. Discrete levels lie at intersections with the dashed curves $b^0_n(\nu)$.

from errors in graphically reading his potential curve U_{sp-} from Fig. 12.)

The $sp-$ potential is quite shallow, even for $R<R_0$. This diminishes the extent of region III of the spectrum, as it does in Fig. 9(a) for $l=2$ of potassium. In fact region III should be quite narrow for any two-electron channel because no more than one bound state will occur in the inner well of a two-electron system (inner-well states correspond to $r_1 \sim r_2$). The limiting behavior in region IV as $\nu \to 0$ is rather different when the long-range field is dipole rather than Coulomb. In the Coulomb problem $\mu^0_{\epsilon a} \to$ integer as $\nu \to 0$, because the regular Coulomb solution has no nodes below $\nu = l+1$. The dipole-field solutions behave instead at small radii as $\sin(a \ln r)$ and therefore have an infinite number of nodes at all energies. These oscillations at small r are unrealistic because no attractive r^{-2} potentials actually extend to $r=0$; these oscillations force $\mu^0_{\epsilon a}$ to diverge as $\nu \to 0$ for any realistic short-range potential.

It is also possible to calculate several useful quantities from QDT as is often done for Rydberg series (Sec. II E of I). In particular the energy dependence of the wave function for $R<R_0$ is mainly localized in its normalization coefficient, Eq. (2.8), which at threshold is just

$$\gamma^{-2}_{\epsilon_n a} \xrightarrow[\nu\to\infty]{} (a/\pi)\nu_n^2 \,. \tag{4.10}$$

Thus the photoabsorption cross sections of successive series members decrease in the ratio

$$\sigma(n+1)/\sigma(n) \sim (\nu_{n+1}/\nu_n)^2 \sim e^{2\pi/a} \,. \tag{4.11}$$

It is also possible to evaluate the mean orbital radius for any given state by noting that $\langle r \rangle_n$ increases with n as

$$\frac{4}{1-e^{-2\pi a}}\,\frac{\pi}{a\nu_n^2}\int_0^\infty dr\, r^2\left[\mathrm{Im}J_{ia}\left(\frac{ir}{\nu_n}\right)\right]^2 \propto \nu_n \,, \tag{4.12}$$

in contrast with Rydberg-series radii, which increase as ν_n^2. For the present example successive bound states occur at $\nu_n = 22, 120, 640, \ldots$, and successive radii in a.u. are roughly $\langle r \rangle_n = 30, 160, 880, \ldots$. While the radii of Rydberg levels increase as a higher power of ν_n than levels in a dipole field, the successive values of ν_n increase much faster for the latter, causing the wave functions $P_n(R)$ to spread out much more rapidly with increasing n. Direct calculation of these wave functions by variational approaches[17] would then require a basis that represents this long-range behavior adequately.

ACKNOWLEDGMENTS

This work owes much to Dr. J. L. Dehmer's suggestion that QDT might be extended to describe atomic core electrons as well as Rydberg electrons, and to several further discussions. I am indebted to Professor U. Fano for continuing guidance and support, and especially for his assistance with the manuscript. Conversations with Dr. M. Inokuti, Dr. C. W. Clark, and M. Kohmoto are also appreciated. The numerical and graphical work were supported by Argonne National Laboratory. Work supported by the Department of Energy, Office of Basic Energy Sciences.

---

[1] U. Fano, C. E. Theodosiou, and J. L. Dehmer, Rev. Mod. Phys. 48, 59 (1976).

[2] C. Greene, U. Fano, and G. Strinati, Phys. Rev. A 19, 1485 (1979).

[3] C. Greene and J. L. Dehmer, Argonne National Laboratory Report No. ANL-77-65 Part I (unpublished).

[4] S. T. Manson, Phys. Rev. 182, 97 (1969); D. C. Griffin, K. L. Andrew, and R. D. Cowan, *ibid.* 177, 62 (1969).

[5] (a) J. H. Macek, J. Phys. B 2, 831 (1968); (b) C. D. Lin, Phys. Rev. A 10, 1986 (1974); (c) C. D. Lin, Phys. Rev. Lett. 35, 1150 (1975); (d) U. Fano, in *Atomic Physics* 1, edited by B. Bederson, V. W. Cohen, and F. M. Pichanick (Plenum, New York, 1969), p. 209; (e) U. Fano and C. D. Lin, in *Atomic Physics* 4, edited by G. zu Pulitz, E. W. Weber, and A. Winnacker (Plenum, New York, 1975), p. 47.

[6] J. A. Armstrong, P. Esherick, and J. J. Wynne, Phys. Rev. A 15, 180 (1977), especially p. 195; also U. Fano (private communication).

[7] M. J. Seaton, Proc. Phys. Soc. Lond. 88, 815 (1966), see especially Fig. 4.

[8] F. Calogero, *Variable Phase Approach to Potential Scattering* (Academic, New York, 1967).

[9] J. L. Dehmer and U. Fano, Phys. Rev. A 2, 304 (1970); C. M. Lee and K. T. Lu, *ibid.* 8, 1241 (1973); A. F. Starace, J. Phys. B 6, 76 (1973).

[10] See, e.g., L. I. Schiff, *Quantum Mechanics*, 3rd ed. (McGraw-Hill, New York, 1968), p. 353.

[11] F. Scheid, *Theory and Problems of Numerical Analysis*, *Schaum's Outline Series* (McGraw-Hill, New York, 1968), p. 232.

[12] F. Herman and S. Skillman, *Atomic Structure Calculations* (Prentice-Hall, Englewood Cliffs, N.J., 1963).

[13] The onset of a nonmonotonic dependence of $b_n^0(\nu)$ on ν accompanies the termination of the pure Coulomb series of levels at $\nu = l+1$. The parameters of Eq. (4.1) are

$$A = \Gamma(\nu + l + 1)/\nu^{2l+1}\,\Gamma(\nu - l)$$

and

$$\mathcal{G} = (2\pi)^{-1}\,\partial A/\partial l.$$

At $\nu = l+1, l+2, \ldots,$ the $\cot\pi\nu$ of Eq. (4.1) diverges, forcing $b_n^0(\nu = \text{integer})$ to be an integer. But at $\nu = l,\ l-1, \ldots, 0$, the zeroes of A cancel these divergences, thereby ending the monotonic ν dependence of $b_n^0(\nu)$. It is the negative values of A in this energy range that cause (f, g) to become imaginary [according to Eq. (27)]; accordingly this pair is inappropriate for $\nu \le l$, as noted in Sec. II E of I.

[14] Experimental values at $\epsilon = 0$ were extrapolated from C. E. Moore, *Atomic Energy Levels*, U. S. Natl. Bur. Stand. Circ. No. 467, (U. S. GPO, Washington, D. C., 1958), Vol. I.

[15] M. Gailitis and R. Damburg, Proc. R. Soc. Lond. 82 192 (1963).

[16] H. C. Bryant *et al.*, Phys. Rev. Lett. 38, 228 (1977); P. A. M. Gram *et al.*, *ibid.* 40, 107 (1978).

[17] J. T. Broad and W. P. Reinhardt, Phys. Rev. A 14, 2159 (1976).

[18] M. Abramowitz and I. A. Stegun, *Handbook of Mathematical Functions* (Dover, New York, 1970), p. 360.